

中国激光

基于高温原位观测的高速风洞内强激光诱导的瞬态 破坏行为研究

马特^{1,2}, 王江涛^{1,2}, 袁武^{1,2,3}, 宋宏伟^{1,2,3*}, 王睿星^{1,2}

¹中国科学院力学研究所流固耦合系统力学重点实验室, 北京 100190;

²中国科学院大学工程科学学院, 北京 100049;

³中国科学院力学研究所空天飞行高温气动国家重点实验室, 北京 100190

摘要 建立了一种适用于强激光辐照面的高温原位观测方法, 并开展了高速风洞内的激光辐照实验, 获得了典型金属材料与复合材料在超声速切向气流条件下的瞬态烧蚀与破坏行为; 此外, 基于 Horn-Schunck 光流法分析了各典型材料的烧蚀特征与质点的运动速度, 基于粒子图像测速法并结合复合材料铺层结构特征获得了瞬时烧蚀速度。研究结果表明, 各材料的动态烧蚀行为有很大差异: 在切向气流作用下, 熔融态钛合金的流动模式从燕尾状转变为羽翼状, 而镍基高温合金则呈雨滴状流动。基于 Kelvin-Helmholtz 机制分析了切向气流作用下不同金属材料击穿时间存在差异的原因。超高温陶瓷复合材料的热化学烧蚀和机械剥蚀特征与编织结构类型密切相关, 并且高激光功率密度条件下的抗激光烧蚀性能与碳纤维含量成正比。

关键词 激光技术; 激光破坏效应; 原位观测技术; 瞬态烧蚀形貌; 超声速切向气流; 光流法

中图分类号 TJ955

文献标志码 A

DOI: 10.3788/CJL221334

1 引言

在高速风洞内开展地面激光破坏实验, 是高速目标激光毁伤机理研究的一种重要手段^[1-3]。强激光辐照下靶材表面迅速升温形成的高温强辐射, 以及激光辐射、高速风洞环境干扰等因素, 导致目前对激光辐照面瞬态烧蚀行为的直接观测还没有实质性进展。通常采用实验结束后对靶材进行测量的方法获取最终的烧蚀形貌、烧蚀深度或平均质量烧蚀速率等数据, 同时利用扫描电镜(SEM)观察材料表面的显微组织特征, 采用能谱分析(EDS)对材料表面的化学成分进行定性和半定量分析, 或用 X 射线衍射(XRD)对材料的相组成进行定性分析, 据此推测出研究对象的激光烧蚀机理^[4-10]。但上述方法无法为激光烧蚀机理研究提供实时可靠的失效演化过程以及相关实验数据。

国内外为了获取材料的瞬态烧蚀形貌开展了一些研究工作, 如: 黄永光等^[11]通过高速摄影技术分析了不同激光功率密度条件下激光辐照碳纤维复合材料的烧蚀行为, 但由于火焰和热解气体的影响没有获得激光辐照区域的烧蚀形貌; 孙翔宇等^[12]利用光学测量技术获得了绝热材料的动态烧蚀特性; Qu 等^[13]在电弧加热

风洞实验中采用原位测量光电系统获得了混合连续纤维(石英纤维、玻璃纤维)增强复合材料的实时烧蚀图像; Sakai 等^[14]设计了一种可以实时原位测量烧蚀界面的烧蚀传感器, 但该系统的测量区域有限; Martin 等^[15]开发了一种 X 射线技术, 用于获取烧蚀材料的实时信息; Gangireddy 等^[16]利用原位显微镜直接观测了 1450~1650 °C 下 ZrB₂-SiC 复合材料的氧化行为; Fang 等^[17]基于实时原位观测技术分析了 1800 °C 氧乙炔焰条件下 SiC 表面二氧化硅液珠的形成、流动和生长机制; Tang 等^[18]为了抑制氧乙炔焰高温下烧蚀试样的辐射, 采用高功率蓝光光源, 并在拍摄相机前安装蓝光带通滤光片, 实现了 C/C 复合材料在 2000 °C 以下烧蚀表面演化的实时捕捉。

不同于氧乙炔焰或电弧加热测试条件下烧蚀材料的正表面, 激光辐照条件下还存在激光反射导致的过度曝光以及温度更加极端等问题(高激光功率密度条件下超高温陶瓷 C/SiC 复合材料的烧蚀温度可达 3000 °C 以上)。所查资料显示, 目前尚未有高速风洞条件下激光诱导高温靶材瞬态烧蚀形貌实验数据的相关报道。本文提出了一种适用于获取激光诱导极端高温下材料烧蚀形貌的原位观测技术, 研究了典型金属材料和复合材料在超声速切向气流条件下的动态烧蚀

收稿日期: 2022-10-17; 修回日期: 2022-11-16; 录用日期: 2022-11-28; 网络首发日期: 2022-12-08

基金项目: 国家自然科学基金(12272379, 11902322)

通信作者: *songhw@imech.ac.cn

行为,通过图像处理分析了研究对象的烧蚀特征并获得了瞬时烧蚀数据。

2 实验系统与原位观测技术

2.1 实验方法

实验系统示意图如图 1 所示,主要包括高能激光器、超声速风洞和原位观测系统。实验用激光器为连续输出光纤激光器(YLS-2000, IPG Photonics 公司,美国),波长为 1070 nm,焦距为 680 mm,焦点处光斑能量均匀分布。实验中所用功率为 2000 W,激光光斑直径为 10 mm,激光功率密度为 2546 W/cm²,激光辐照时间为 4 s。超声速风洞采用中国科学院力学研究所高温气体动力学国家重点实验室的直连式超声速燃烧实验台,其主要由加热器、喷管、实验段及气路供应系统、控制台、测量系统组成,实验测试区包括试件装载区以及测量窗口,其中观察窗口材料为光学石英玻璃。选择光学石英玻璃作为观察窗口材料主要有以下两个原因:1)相比于普通玻璃,光学石英玻璃具有更高的使用温度,可在 1100 °C 条件下长时间使用;2)光学石英玻璃在紫外线到红外线的整个光谱波段均具有更好的透光性能,可见光透过率在 93% 以上,红外线光谱区透过率可达 90% 以上,使用光学石英玻璃能够获得更好的测量结果。该风洞可提供马赫数为 1.8~4.0 之间的超声速气流环境。此次实验主要研究马赫数为 3.0 的高速气流对烧蚀行为的影响,气流总温度和总压力分别为 815 K 和 1850 kPa。

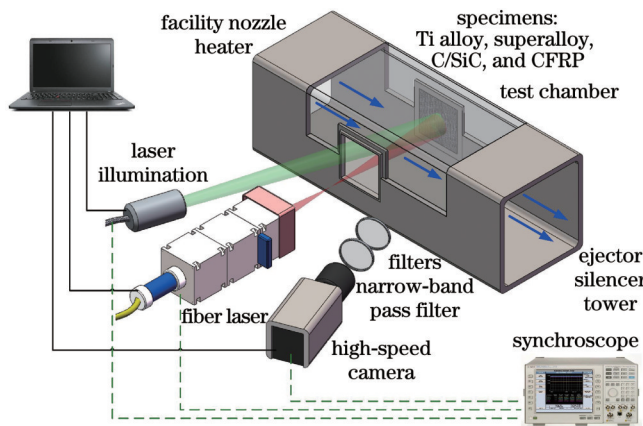


图 1 实验系统示意图

Fig. 1 Schematic of experimental setup

获取材料激光辐照面动态烧蚀过程的难点主要在于如何避免激光反射以及材料在激光诱导高温条件下的强辐射所导致的图像过度曝光。为了解决以上问题,实验中采用由高速摄像机、辅助照明系统、衰减片和窄带通滤光片组成的原位观测系统。其中的辅助照明系统可以提供不同于高能激光波长的背景光源,实验中采用该系统并结合窄带通滤光片来避免激光反射并降低高温强辐射对图像采集的影响。虽然

窄带通滤光片可以抑制其余波长光线对高速摄像机拍摄的影响,但其本波长范围内的辐射仍可使图像过度曝光,所以还需结合衰减片来降低辐射强度从而获得清晰图像。实验中使用的是 Vision Research 公司生产的 Phantom v2012 高速摄像机,其采样频率为 100 Hz,分辨率为 1280 pixel×800 pixel。辅助照明系统的波长为 810 nm,光源功率为 200 W。窄带通滤光片的中心波长为 810 nm,带宽(半峰全宽)为 10 nm,光密度(OD)值为 OD3。衰减片选择 ND64。在实验过程中,高能激光系统、辅助照明系统和高速摄像机通过数字延迟/脉冲发生器(作为时序控制器)实现统一触发和启动,从而保证采样时间的一致性。实验前,激光器及测量设备均处于外触发模式。首先运行风洞,待风洞稳定出风后,统一触发激光器与原位观测系统。

2.2 图像处理方法

瞬时烧蚀物理图像可为各类图像处理方法获取更多的烧蚀数据提供基础,如王福斌等^[19]基于瞬时烧蚀物理图像,采用改进的小波阈值滤噪和 K 均值聚类分割图像处理方法获得了飞秒激光诱导的有效光斑区域。本团队采用光流法分析了各典型材料的烧蚀特征与质点运动速率,然后采用粒子图像测速法(PIV 法)并结合复合材料的铺层结构特征获得了瞬时烧蚀速率。

光流法作为运动目标的检测方法,可利用序列图像灰度随时间的变化来确定物体结构及其运动状态^[20]。将光流法应用于激光破坏效应研究中,可以分析激光诱导的温度场变化、热变形、烧蚀形貌演变以及高速气流剥蚀作用引起的物质运动速度。光流法的基本原理如下:

设 t 时刻像素点 (x, y) 处的灰度值为 $I(x, y, t)$;在 $t + \Delta t$ 时刻,该像素点更新到位置 $(x + \Delta x, y + \Delta y)$,灰度值更新为 $I(x + \Delta x, y + \Delta y, t + \Delta t)$ 。根据灰度对时间不变原理可得

$$I(x, y, t) = I(x + \Delta x, y + \Delta y, t + \Delta t), \quad (1)$$

通过泰勒公式将上式展开得

$$I(x + \Delta x, y + \Delta y, t + \Delta t) = I(x, y, t) + \frac{\partial I}{\partial x} \cdot \frac{\Delta x}{\Delta t} + \frac{\partial I}{\partial y} \cdot \frac{\Delta y}{\Delta t} + \frac{\partial I}{\partial t} + \epsilon, \quad (2)$$

式中: ϵ 代表泰勒公式展开后的高阶项。然后将沿 x 方向和 y 方向的光流矢量分量 $u(x, y, t)$ 和 $v(x, y, t)$ 代入式(2),并忽略高阶项,可得光流场的基本控制方程

$$I_x u + I_y v + I_t = 0. \quad (3)$$

由于光流场中有两个变量,但却只有一个基本控制方程,因此无法求出唯一解。Horn 和 Schunck 提出了一种用光流的全局平滑性假设来求解光流的方法,即 Horn-Schunck 算法。 u 和 v 的求解公式为

$$\begin{cases} u^{(n+1)} = \bar{u}^n - I_x \frac{I_x \bar{u}^{(n)} + I_y \bar{v}^{(n)} + I_t}{\lambda + I_x^2 + I_y^2}, \\ v^{(n+1)} = \bar{v}^n - I_y \frac{I_x \bar{u}^{(n)} + I_y \bar{v}^{(n)} + I_t}{\lambda + I_x^2 + I_y^2}, \end{cases} \quad (4)$$

式中: λ 为平滑度的约束参数; n 代表迭代次数。

粒子图像测速法常用于流场速度的测量。进行多次摄像,以记录流场中粒子的位置,进而分析并测出流动速度。对于一些离散固体,比如沙砾,通过该测速法也可以获得沙砾质点的流动速度^[21]。本文以复合材料中的纤维作为示踪粒子,计算纤维的瞬时运动速度。首先将获取到的烧蚀图像导入开源软件 MATLAB 工具箱 PIVlab 中,然后选取图像上约 5 mm×5 mm 的激光辐照中心区域进行分析。数据分析过程中使用 3 次传递:第 1 次传递 128 pixel,第 2 次传递 64 pixel,第 3 次传递 32 pixel。通过高通滤波器去除图像中的低频噪点信息,最后得到纤维运动速度矢量云图。

2.3 实验材料

为了验证原位观测技术在激光诱导的极端高温环境中的适用性,选取两种典型的金属材料和两种典型的复合材料作为研究对象,前者包括钛合金和镍基高温合金,后者包括超高温陶瓷 C/SiC 复合材料和碳纤维增强环氧树脂 CFRP 层合板。其中:钛合金牌号为 TC4,镍基高温合金牌号为 GH625,两种试件的尺寸均为 50 mm×50 mm×2 mm;C/SiC 复合材料有两种结构,一种是二维(2D)编织结构,另一种是三维针刺(3DN)结构,增强相均为 T300 碳纤维,均采用化学气浸渗(CVI)工艺制备得到,并且试件表面沉积了厚度约为 50 μm 的 SiC 涂层,试件尺寸均为 50 mm×50 mm×2 mm,基本性能参数如表 1 所示;CFRP 复合材料的增强相为 T700 碳纤维,基体 BA9916 是高温(180 °C)固化高韧性环氧树脂,铺层方式为 [45°, 0°, -45°, 90°]_{2S},共计 16 层,每层厚度为 0.15 mm,试件尺寸为 50 mm×50 mm×2.4 mm,基本性能参数如表 2 所示。

表 1 C/SiC 复合材料的基本性能参数
Table 1 Basic performance parameters of C/SiC composite

Composite	Density / (g·cm ⁻³)	Porosity / %	Bending strength / MPa	Bending modulus / GPa	Fracture toughness / (MPa·m ^{1/2})
2D C/SiC	2.0	13	539±39		22.3±1.0
3DN C/SiC	2.1	18	242±38	46±10	18.0±7.0

表 2 T700/BA9916 CFRP 复合材料的主要物理、力学性能

Table 2 Main physical and mechanical properties of T700/BA9916 CFRP composite

Physical and mechanical properties		Value
Physical property	Mass fraction of matrix / %	38±3
	Density of matrix / (g·cm ⁻³)	1.30±0.04
	Density of fiber / (g·cm ⁻³)	1.78±0.04
	Mass fraction of volatile / %	≤1.5
	Porosity / %	≤1.5
	Lamina thickness / mm	0.15±0.015
Mechanical property	0° tensile strength / MPa	1489
	0° tensile modulus / GPa	132.8
	90° tensile strength / MPa	58.5
	90° tensile modulus / GPa	9.7
	Shear strength / MPa	121
	Shear modulus / GPa	5.3

3 结果与讨论

3.1 典型金属材料的激光破坏行为

钛合金在超声速切向气流条件下的激光破坏过程如图 2 所示。图 2 中各分图的上图是原位观测系统获

取到的瞬时烧蚀形貌,下图是基于 Horn-Schunck 光流法获得的计算结果。由光流法基本原理可知,最终的计算结果代表了序列图像灰度随时间的变化,所以在高速切向气流条件下的激光烧蚀过程中,激光诱导的温度升高、材料发生相变后表面状态的改变、切向气流引起的机械剥蚀效应导致的物质流动等现象,都会导致序列图像的灰度发生变化,所以光流法获得的灰度变化速度云图所代表的物理含义就需要根据实际物理现象进行具体分析。

由图 2(a)可以看出:当激光辐照 0.4 s 时,通过光流法计算得到的结果显示仅在激光辐照区域有光流速度,结合原位观测结果可知此时主要是钛合金的温度场导致的图像灰度变化。当激光辐照时间延长至 0.8 s 时,如图 2(b)所示,激光辐照区域的钛合金开始发生相变,此时可将钛合金的激光烧蚀区域分为激光辐照中心区域、黑色过渡区域以及白色边缘区域三个典型区域;在超声速切向气流作用下,熔融态钛合金开始沿气流方向流动,根据光流计算结果可知白色边缘区域之外的热影响区范围变大。随着激光与气流的持续作用,如图 2(c)所示,除了热影响区继续扩大以外,熔融态钛合金也在机械剥蚀效应作用下被剥离出激光辐照区域,并且尾迹区域呈燕尾状流动,即熔融态钛合金仅在光斑区域的上下两侧流动;光流结果中燕尾的速度分布代表了熔体在两帧序列图像内的平均流动速度。当激光辐照时间增加至 1.6 s 时,如图 2(d)所示,钛合

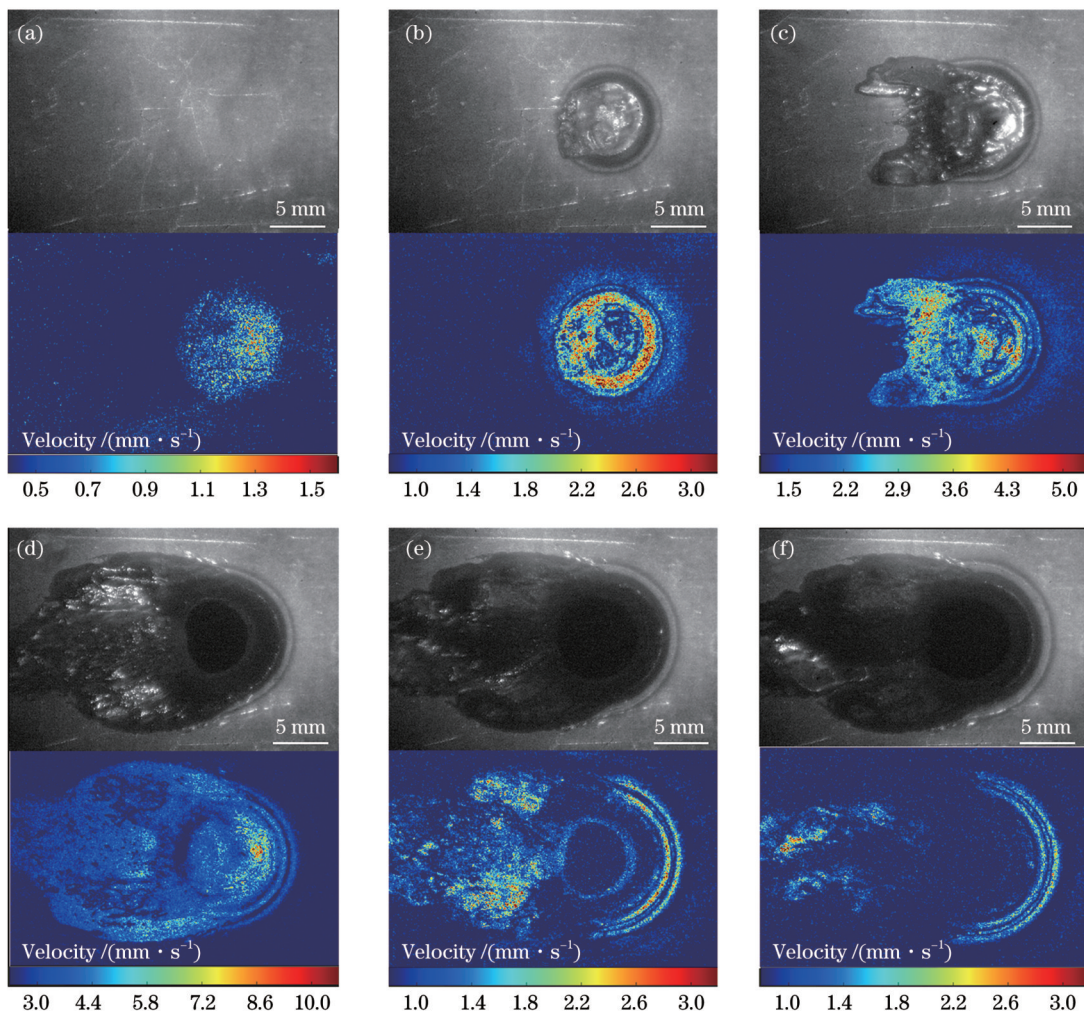


图2 钛合金在激光辐照与超声速切向气流条件下的动态烧蚀形貌(每幅图中的上图为原位观测结果,下图为光流法处理结果)。
(a)0.4 s;(b)0.8 s;(c)1.2 s;(d)1.6 s;(e)2.0 s;(f)2.4 s

Fig. 2 Dynamic laser ablation morphology of Ti alloy exposed to laser irradiation and supersonic tangential airflow (the figure includes two parts: upper figure is obtained by *in-situ* observation technology, lower figure is obtained by optical flow method). (a) 0.4 s; (b) 0.8 s; (c) 1.2 s; (d) 1.6 s; (e) 2.0 s; (f) 2.4 s

金已经出现了穿孔,并且尾迹区域的熔体流动模式也发生了变化,即光斑中心母线上的熔体流动速度高于燕尾两侧的流动速度,最终形成了激光破坏效应研究中常见的羽翼状尾迹区。钛合金后续的烧蚀行为[如图2(e)和图2(f)所示]主要以热影响区和穿孔尺寸的变化为主,特别是图2(f)所示光流结果右侧由热扩散导致的过渡区域以及边缘区域的变化速度较为明显,中心区域穿孔尺寸的变化速度较小,而尾迹区的变化速度也开始减小。以上分析结果进一步说明了获取研究对象瞬时烧蚀行为的重要性:不仅可以明确激光诱导的动态变化过程,还可以为机理分析以及相应的数值模拟提供更充分、更直观的验证性数据。

镍基高温合金在激光与超声速气流联合作用下的瞬时烧蚀行为如图3所示。激光辐照时间为0.4 s以及0.8 s时,如图3(a)和图3(b)所示,与钛合金的激光烧蚀行为类似,镍基高温合金仅表现为温度场发生变化以及激光辐照区域开始呈现为熔融态。激光辐照时间

为1.2 s时,镍基高温合金的尾迹区明显不同于钛合金,其形貌主要表现为尖笋状。镍基高温合金熔体在机械剥蚀作用下的流动模式也与钛合金有较大区别:钛合金熔体的流动模式类似于火山喷发后熔浆的流动,比较连续;而镍基高温合金熔体的流动模式则类似于暴风中离散雨滴的流动,受重力的影响比较显著,如图3(d)、(e)、(f)所示,尾迹区明显向下偏移,且有较多的熔体零散地凝固在尾迹区周围。

钛合金与镍基高温合金这两种典型金属材料在激光与切向气流耦合作用下的击穿时间为1.32 s和1.44 s,最终穿孔直径分别为7.23 mm和5.72 mm。造成流动模式以及击穿时间差异的原因主要在于两者不同的熔体表面不稳定性。根据 Kelvin-Helmholtz 机制^[22],当切向气流的能量耦合到激光诱导的熔融态表面时,会形成不稳定的毛细波,随着时间延长,毛细波的波顶形成液体小珠,而液体小珠会被切向气流挟带移走。该机制主要与材料的表面张力、密度正相关,即

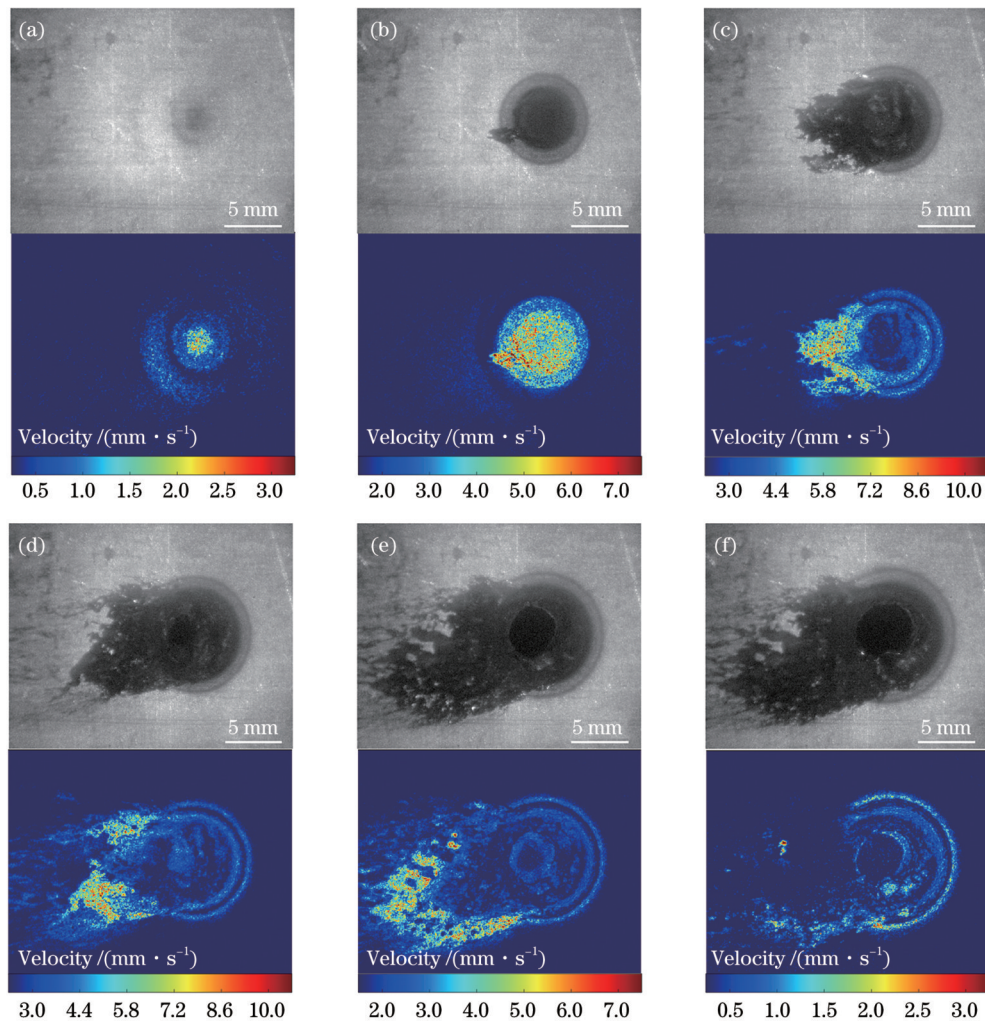


图3 镍基高温合金在激光辐照与超声速切向气流条件下的动态烧蚀形貌(每幅图中的上图为原位观测结果,下图为光流法处理结果)。(a)0.4 s;(b)0.8 s;(c)1.2 s;(d)1.6 s;(e)2.0 s;(f)2.4 s

Fig. 3 Dynamic laser ablation morphology of Ni-based superalloy exposed to laser irradiation and supersonic tangential airflow (the figure includes two parts: upper figure is obtained by *in-situ* observation technology, lower figure is obtained by optical flow method). (a) 0.4 s; (b) 0.8 s; (c) 1.2 s; (d) 1.6 s; (e) 2.0 s; (f) 2.4 s

材料呈熔融态时的表面张力和密度越大,气流加速击穿的作用越小。因此,虽然钛合金 TC4 的熔点(1670°C)高于镍基高温合金 GH625 的熔点(1340°C),但在切向气流条件下高密度的镍基高温合金反而具有更好的抗激光击穿性能。

3.2 典型复合材料的激光破坏行为

2D C/SiC 复合材料在超声速切向气流条件下的激光破坏过程如图 4 所示。从实验结果中可以清晰地看到二维编织结构的烧蚀演变过程、激光辐照边缘区域二氧化硅液滴的形成与迁移,以及白色尾迹区的形成过程。清晰的动态烧蚀过程说明了该极端高温原位观测技术不仅适用于金属材料,还可用于复合材料烧蚀行为的观测。

由图 4(a)可知激光辐照 0.4 s 时,2D C/SiC 复合材料的激光烧蚀中心区域已有碳纤维编织结构暴露在环境中,说明 SiC 涂层在此时已发生主动氧化或热分解反应,失去抗氧化能力。在激光能量持续输入与切

向气流引起的机械剥蚀效应的耦合作用下,碳纤维层开始出现明显的逐层剥离,并且剥蚀形貌以片状剥蚀为主^[23],如图 4(b)、(c)、(d)所示。由光流云图结果可以看出,烧蚀形貌的变化主要发生在激光辐照中心区域,如图 4(c)所示,光流结果中激光辐照中心灰度的变化最为显著,对应的原位观测结果则显示该区域的灰度明显高于其他区域。造成以上现象的主要原因是位于上层的复合材料在片状剥蚀作用下被瞬间剥离,导致激光辐照面温度不连续。如图 4(e)和图 4(f)所示,当激光辐照时间增加至 2.0 s 之后,烧蚀特征以热影响区以及烧蚀中心区域直径扩大为主,但烧蚀深度方向不再呈现明显的逐层变化,而是表现为以碳纤维氧化或升华为主的碳纤维束退化过程。光流结果图也体现了以上特点,灰度变化云图呈现为与编织结构相关的散点状分布。造成以上烧蚀现象的原因是机械剥蚀效应不仅与温度、来流速度的大小有关,还与烧蚀区域内气流流动模式有关^[24],即:流动模式为闭式流动时,机

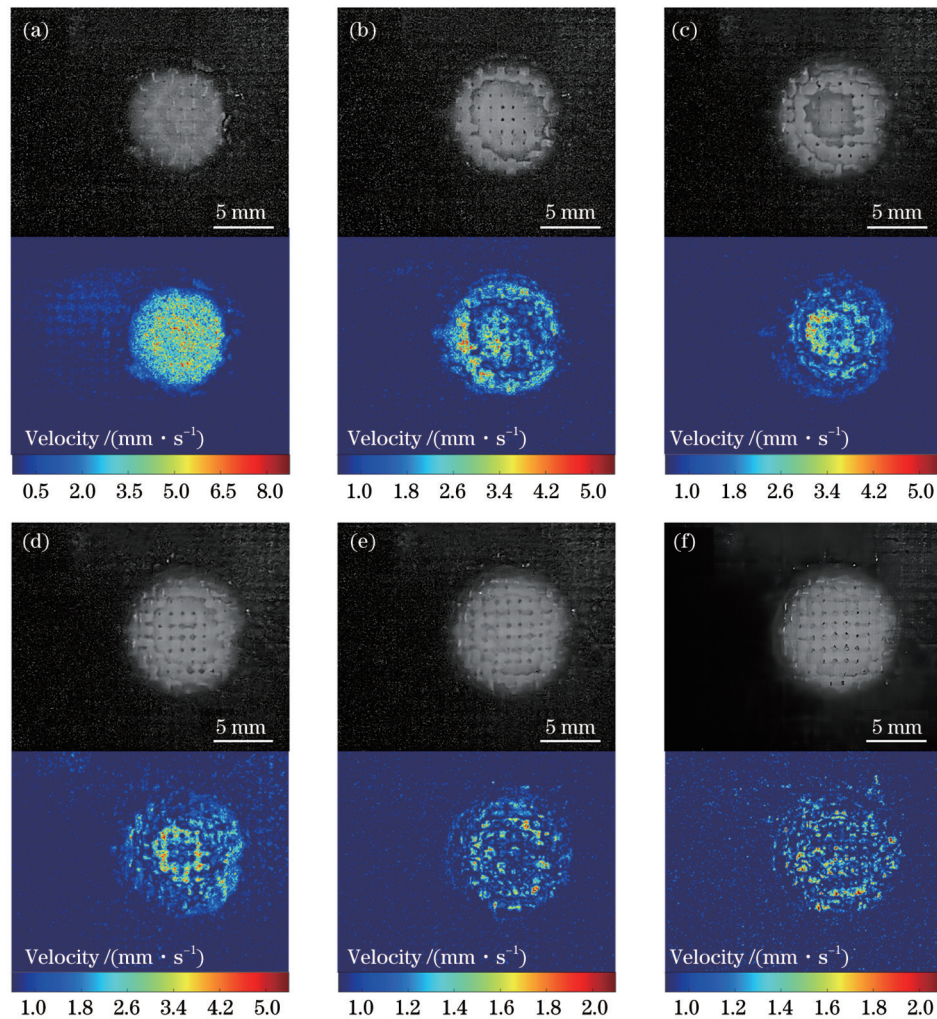


图4 2D C/SiC复合材料在激光辐照与超声速切向气流条件下的动态烧蚀形貌(每幅图中的上图为高速摄影获取的结果,下图为光流法处理结果)。(a)0.4 s;(b)0.8 s;(c)1.2 s;(d)1.6 s;(e)2.0 s;(f)2.4 s

Fig. 4 Dynamic laser ablation morphology of 2D C/SiC composite exposed to laser irradiation and supersonic tangential airflow (the figure includes two parts: upper figure is obtained by *in-situ* observation technology, lower figure is obtained by optical flow method). (a) 0.4 s; (b) 0.8 s; (c) 1.2 s; (d) 1.6 s; (e) 2.0 s; (f) 2.4 s

械剥蚀效应较为明显;当流动模式转变为开式流动后,机械剥蚀作用开始减弱。随着激光辐照时间增加,辐照面的温度逐渐升高,从而使得后续的激光烧蚀行为以升华机制为主导^[25]。

图5给出了3DN C/SiC复合材料在激光辐照和超声速切向气流条件下的激光破坏过程。从图中可以明显地观察到3DN C/SiC复合材料纤维层结构的变化。三维针刺碳纤维预制体的制造工艺是:先将碳纤维制成胎网层和无纬布(碳纤维丝束中的单丝数量为12000根),然后将单层90°无纬布、胎网层、0°无纬布等依次循环叠加,然后进行针刺。根据设计厚度,经反复叠层、针刺,最终形成了三维针刺碳纤维预制体。所以从烧蚀0.4 s到烧蚀1.2 s,烧蚀行为主要发生在第一层90°无纬布层,如图5(a)到图5(c)所示;当激光辐照时间达到1.6 s时,如图5(d)所示,激光辐照中心区域的90°无纬布层已退化断裂,并有胎网层开始裸露;在图5(e)和图5(f)中,即激光辐照时间为2.0 s和2.4 s时,开始裸

露出0°无纬布。

不同的编织结构会使C/SiC复合材料的动态烧蚀行为出现差异,同时它们的烧蚀深度也有所不同:2D C/SiC复合材料的烧蚀深度为1.13 mm,而3DN C/SiC复合材料的烧蚀深度为1.23 mm。主要原因在于两者的热物性参数以及碳纤维含量不同。相比于2D C/SiC复合材料,3DN C/SiC复合材料在厚度方向上的热导率更大,导致其温度明显高于2D C/SiC,所以其热化学烧蚀速率也会高于2D C/SiC。同时,在激光功率密度为2546 W/cm²的辐照条件下,激光辐照中心区域很快达到SiC基体的热分解反应温度,甚至达到碳的升华温度。升华反应为吸热过程,碳纤维含量越高,能够吸收的激光能量越多,所以此时C/SiC复合材料的抗烧蚀性能还取决于碳纤维含量。3DN C/SiC中碳纤维的质量分数(36.0%)要小于2D C/SiC中碳纤维的质量分数(54.2%),因此其烧蚀深度大于2D C/SiC。

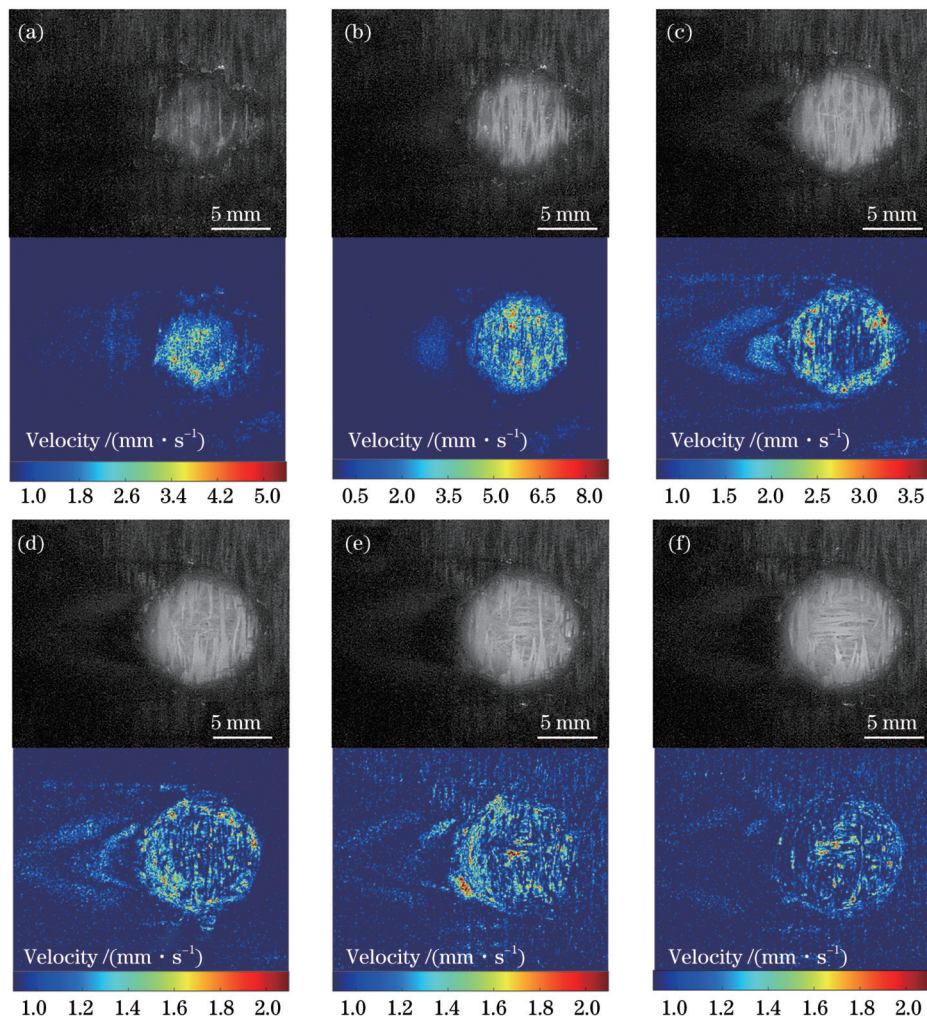


图 5 3DN C/SiC 复合材料在激光辐照与超声速切向气流条件下的动态烧蚀形貌(每幅图中的上图为高速摄影获取的结果,下图为光流法处理结果)。(a)0.4 s;(b)0.8 s;(c)1.2 s;(d)1.6 s;(e)2.0 s;(f)2.4 s

Fig. 5 Dynamic laser ablation morphology of 3DN C/SiC composite exposed to laser irradiation and supersonic tangential airflow (the figure includes two parts: upper figure is obtained by *in-situ* observation technology, lower figure is obtained by optical flow method). (a) 0.4 s; (b) 0.8 s; (c) 1.2 s; (d) 1.6 s; (e) 2.0 s; (f) 2.4 s

3.3 基于粒子图像法获取瞬时烧蚀速率

图 6 给出了超声速气流为 Ma 3.0、激光功率为 1000 W(激光功率密度为 1273 W/cm^2)时 CFRP 复合材料的动态烧蚀过程,从中可以清晰地看到 CFRP 复合材料在烧蚀过程中的铺层变化:激光辐

照 0.8 s 时,裸露的碳纤维铺层角度为 45° ,1.6 s 时转变为 0° ,2.4 s 时转变为 -45° ,4.0 s 时铺层角度已转变成了 90° 。

裸露纤维铺层角度的变化说明了 CFRP 复合材料的烧蚀深度在逐渐变化。以纤维作为参考粒子,

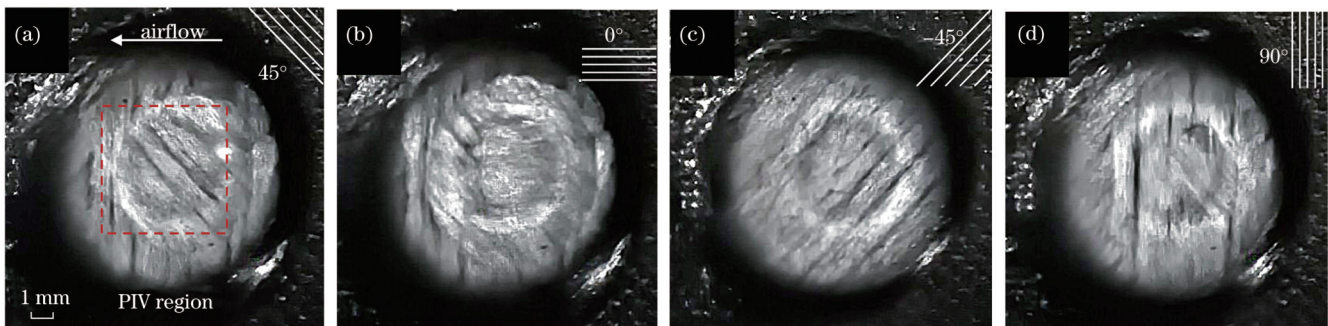


图 6 CFRP 复合材料在激光辐照与超声速切向气流条件下的动态烧蚀形貌。(a)0.8 s;(b)1.6 s;(c)2.4 s;(d)4.0 s

Fig. 6 Dynamic laser ablation morphology of CFRP composite exposed to laser irradiation and supersonic tangential airflow. (a) 0.8 s; (b) 1.6 s; (c) 2.4 s; (d) 4.0 s

基于 PIVlab 获得了 CFRP 的瞬时烧蚀深度, 所选计算区域为图 6(a)中的虚线框区域, 计算结果如图 7(a)所示。图 7(a)中的速度矢量云图代表了不同铺设角度下纤维的运动方向, 当速度矢量方向发生变化时, 即认为 CFRP 复合材料中的单层已经完全烧蚀, 此时记录一次烧蚀深度, 从而获得瞬时烧蚀深度。不同于实验后测量获得的线性平均烧蚀速率, 基于上述方法获得的瞬时烧蚀深度呈明显的非线性特征。由图 7(b)所

示的瞬时烧蚀深度可知, 复合材料在超声速切向气流下的激光烧蚀深度与激光功率密度、来流速度均相关: 当激光功率密度为 1273 W/cm^2 、来流速度为马赫数 1.8 时, 烧蚀深度为 0.36 mm; 当激光功率密度为 1273 W/cm^2 、来流速度增加至马赫数 3.0 时, 烧蚀深度增加至 0.47 mm; 当激光功率密度增加至 2546 W/cm^2 、来流速度为马赫数 3.0 时, 烧蚀深度增加至 1.07 mm。这说明激光功率密度对激光烧蚀行为的影响更大。

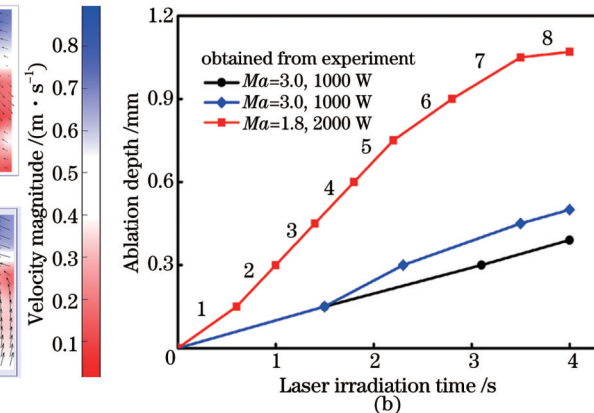
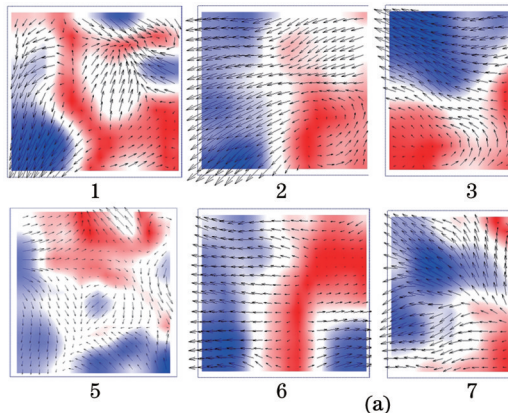


图 7 CFRP 复合材料在超声速切向气流作用下的激光烧蚀行为。(a)速度矢量云图;(b)不同功率和马赫数下的瞬时烧蚀深度
Fig. 7 Laser ablation behavior of CFRP composite subjected to supersonic tangential airflow. (a) Velocity vector chart; (b) instantaneous laser ablation depth under different laser power densities and Mach numbers

4 结 论

本文提出一种极端高温激光烧蚀原位观测技术, 并采用该技术获得了超声速切向气流作用下激光诱导的典型金属和复合材料的动态烧蚀形貌, 清晰的瞬时烧蚀图像为理解复杂的激光烧蚀机理提供了更加直观的支撑性数据。通过图像处理方法获取更多的实时烧蚀数据, 可以准确地分析不同金属材料熔融尾迹区域的形成过程与形貌差异, 例如钛合金尾迹区从燕尾状转变为羽翼状的过程以及镍基高温合金的雨滴状流动过程。基于 Horn-Schunck 光流法还能获得尾迹区熔融态金属的流动以及热影响区的扩散特征。复合材料的烧蚀行为与其增强相编织结构有关: 2D C/SiC 复合材料的机械剥蚀效应以片状剥蚀为主, 而 3DN C/SiC 以及 CFRP 复合材料以纤维逐层剥蚀为主。此外, 基于粒子图像速度法并以不同铺层方向纤维的运动方向为判据, 获得了 CFRP 复合材料的瞬时烧蚀深度。通过以上分析可知, 本文所提原位观测技术在极端高温工程, 特别是激光破坏效应研究中具有广阔的应用前景。

参 考 文 献

- [1] Zhao W N, Ma T, Song H W, et al. Effects of tangential supersonic airflow on the laser ablation of laminated CFRP[J]. Journal of Materials Research and Technology, 2021, 14: 1985-1997.
- [2] 陈敏孙, 江厚满, 焦路光, 等. 切向气流作用下玻璃纤维复合材料的激光辐照效应[J]. 强激光与粒子束, 2013, 25(5): 1075-1080.
- [3] Peng G L, Zhang X H, Gao Y J, et al. Influence of plume on transmittivity during laser irradiating carbon/epoxy composites in gas flow[J]. Chinese Journal of Lasers, 2015, 42(2): 0206004.
- [4] Fan X M, Yin X W, Cao X Y, et al. Improvement of the mechanical and thermophysical properties of C/SiC composites fabricated by liquid silicon infiltration[J]. Composites Science and Technology, 2015, 115: 21-27.
- [5] Tong Y G, Bai S X, Hu Y L, et al. Laser ablation resistance and mechanism of Si-Zr alloyed melt infiltrated C/C-SiC composite[J]. Ceramics International, 2018, 44(4): 3692-3698.
- [6] Wang J T, Ma Y Z, Song H W, et al. Experimental investigation on laser ablation of C/SiC composites subjected to supersonic airflow[J]. Optics & Laser Technology, 2019, 113: 399-406.
- [7] Allheily V, Lacroix F, Eichhorn A, et al. An experimental method to assess the thermo-mechanical damage of CFRP subjected to a highly energetic $1.07 \mu\text{m}$ -wavelength laser irradiation [J]. Composites Part B: Engineering, 2016, 92: 326-331.
- [8] Li X, Hou W T, Han B, et al. Thermal response during volumetric ablation of carbon fiber composites under a high intensity continuous laser irradiation[J]. Surfaces and Interfaces, 2021, 23: 101032.
- [9] 邓泽超, 刘建东, 王旭, 等. 真空环境中脉冲激光烧蚀制备纳米银晶薄膜的生长特性[J]. 中国激光, 2019, 46(9): 0903003.
- [10] Deng Z C, Liu J D, Wang X, et al. Growth characteristics of Ag nanocrystalline thin films prepared by pulsed laser ablation in vacuum[J]. Chinese Journal of Lasers, 2019, 46(9): 0903003.
- [10] 林嘉剑, 明瑞, 李学坤, 等. 飞秒激光烧蚀面齿轮材料的形貌特征研究[J]. 中国激光, 2021, 48(14): 1402017.
- [11] Lin J J, Ming R, Li X K, et al. Study on morphology

- characteristics of femtosecond laser-ablated face gear materials[J]. Chinese Journal of Lasers, 2021, 48(14): 1402017.
- [11] 黄永光, 刘世炳, 龙连春, 等. Nd:YAG 连续激光烧蚀碳纤维复合材料的过程观测[J]. 中国激光, 2008, 35(12): 2042-2046. Huang Y G, Liu S B, Long L C, et al. Observation on the process of continuous-wave Nd:YAG laser ablation on carbon fiber composite material[J]. Chinese Journal of Lasers, 2008, 35(12): 2042-2046.
- [12] 孙翔宇, 张炜, 胡淑芳, 等. 绝热材料动态烧蚀试验方法[J]. 推进技术, 2011, 32(4): 597-600. Sun X Y, Zhang W, Hu S F, et al. Methodology of dynamic ablation test for insulation material[J]. Journal of Propulsion Technology, 2011, 32(4): 597-600.
- [13] Qu Z, Wang X, Tang Y L, et al. *In situ* visualization measurement of flat plate ablation in high-temperature gas flow[J]. Journal of Applied Mechanics, 2018, 85(6): 061006.
- [14] Sakai T, Nakazawa H, Dantsuka Y, et al. Dual-component sensor design for *in situ* ablation measurement[J]. Journal of Thermophysics and Heat Transfer, 2016, 31(2): 307-317.
- [15] Martin H T, Cortopassi A C, Kuo K K. Assessment of the performance of ablative insulators under realistic solid rocket motor operating conditions[J]. International Journal of Energetic Materials and Chemical Propulsion, 2017, 16(1): 1-22.
- [16] Gangireddy S, Karlsson S N, Norton S J, et al. *In situ* microscopy observation of liquid flow, zirconia growth, and CO bubble formation during high temperature oxidation of zirconium diboride-silicon carbide[J]. Journal of the European Ceramic Society, 2010, 30(11): 2365-2374.
- [17] Fang X F, Qu Z, Zhang C X, et al. *In-situ* testing of surface evolution of SiC during thermal ablation: mechanisms of formation, flowing and growth of liquid silica beads[J]. Ceramics International, 2017, 43(9): 7040-7047.
- [18] Tang Y L, Zhang J S, Yun M K, et al. High-frequency flashing of light source for synchronous measurement of temperature and deformation at elevated temperature[J]. Optics and Lasers in Engineering, 2021, 137: 106361.
- [19] 王福斌, 孙志林. 飞秒激光烧蚀光斑的亮度特征及分形维数[J]. 激光与光电子学进展, 2021, 58(24): 2432001. Wang F B, Sun Z L. Brightness characteristics and fractal dimension of spot ablated by femtosecond laser[J]. Laser & Optoelectronics Progress, 2021, 58(24): 2432001.
- [20] 管飞, 王荣. 基于 Horn-Schunck 光流法的运动目标检测的研究[J]. 仪表技术, 2015(2): 43-45. Guan F, Wang R. Research on moving object detection based on Horn-Schunck optical flow algorithm[J]. Instrumentation Technology, 2015(2): 43-45.
- [21] Thielicke W, Stamhuis E J. PIVlab – towards user-friendly, affordable and accurate digital particle image velocimetry in MATLAB[J]. Journal of Open Research Software, 2014, 2: 1-10.
- [22] Johnson R L, O'Keefe J D. Laser burnthrough time reduction due to tangential airflow: an interpolation formula[J]. AIAA Journal, 1974, 12(8): 1106-1109.
- [23] 黄海明, 杜善义, 吴林志, 等. C/C 复合材料烧蚀性能分析[J]. 复合材料学报, 2001, 18(3): 76-80. Huang H M, Du S Y, Wu L Z, et al. Analysis of the ablation of C/C composites[J]. Acta Materiae Compositae Sinica, 2001, 18(3): 76-80.
- [24] Wang J T, Ma T, Wang Z, et al. Three-dimensional flow structures and heat transfer characteristics of compressible flow over a cylindrical cavity[J]. Aerospace Science and Technology, 2022, 122: 107408.
- [25] Wang Z, Wang J T, Song H W, et al. Laser ablation behavior of C/SiC composites subjected to transverse hypersonic airflow[J]. Corrosion Science, 2021, 183: 109345.

High Temperature *In-Situ* Observation of High-Power Laser Induced Instantaneous Damage Behavior in High-Speed Wind Tunnel

Ma Te^{1,2}, Wang Jiangtao^{1,2}, Yuan Wu^{1,2,3}, Song Hongwei^{1,2,3*}, Wang Ruixing^{1,2}

¹Key Laboratory for Mechanics in Fluid Solid Coupling Systems, Institute of Mechanics, Chinese Academy of Sciences, Beijing 100190, China;

²School of Engineering Science, University of Chinese Academy of Sciences, Beijing 100049, China;

³State Key Laboratory of High Temperature Gas Dynamics, Institute of Mechanics, Chinese Academy of Sciences, Beijing 100190, China

Abstract

Objective Laser damage experiment in the high-speed wind tunnel is an important method for studying the mechanism of high-speed targets exposed to laser irradiation. There is no substantive progress in the instantaneous ablative behavior of laser-irradiated surfaces owing to the high-temperature radiation coupled with factors such as laser radiation and high-speed wind tunnel environment interference. The conventional methods are used to obtain data, such as the final ablation morphology, ablation depth, or average mass ablation rate, after the experiment. However, the traditional methods cannot provide instantaneous and reliable failure evolution process or real-time experimental data. The temperature of the specimens under laser irradiation was extremely high. For instance, the temperature of ceramic-based composites can exceed 3000 °C under a high laser power density. The experimental data on the instantaneous ablative morphology of high-temperature targets exposed to laser irradiation and supersonic tangential airflow have not been reported until now. In the present study, we propose an *in-situ* observation technology suitable for obtaining the instantaneous laser-irradiated ablative morphology of different materials. The real-time ablative behaviors of the metals and composite materials under supersonic tangential airflow were captured. The ablative characteristics of the specimens were analyzed using image processing methods, and instantaneous ablative data were obtained.

Methods Titanium alloy, nickel-based superalloy, ceramic-based C/SiC, and carbon fiber-reinforced polymer CFRP composites are studied in this paper. First, an *in-situ* observation platform suitable for laser-irradiated extreme high-temperature environments

was established, which mainly composed of a high-speed camera, auxiliary lighting system, attenuating filter, and narrow band-pass filter. Subsequently, laser damage experiments were conducted in a supersonic wind tunnel. The experiment employed a supersonic wind tunnel facility at the State Key Laboratory of High-Temperature Gas Dynamics (LHD) of the Institute of Mechanics, Chinese Academy of Sciences. It operates on the oxygen-hydrogen combustion principle and can provide a free stream of Mach number 1.8–4.0 in the test section. It comprises heaters, nozzles, air supply systems, consoles, and a measurement system. In the experiments, the tangential supersonic airflow was set to Mach number 3.0. The total temperature and pressure of the gas flow were 815 K and 1850 kPa, respectively. Finally, the optical flow method was used to analyze the ablative characteristics and particle motion velocity of each material, and the instantaneous ablation rate was obtained using the PIV method combined with the structural characteristics of the composite material layup.

Results and Discussions The burn-through behaviors of titanium alloy and nickel-based superalloy were obtained. The burn-through time under the coupled action of laser and tangential airflow are 1.32 s and 1.44 s, respectively. The final perforation diameters are 7.23 mm and 5.72 mm, respectively. The difference in the flow pattern and burn-through time is attributed to the instability of the melt surface. According to the Kelvin-Helmholtz theory, the mechanism of the burn-through behavior is mainly related to the surface tension and density of the material. Although the melting point of the titanium alloy TC4 (1670 °C) is higher than that of the nickel-based superalloy GH625 (1340 °C), the high-density nickel-based superalloy exhibits better resistance to laser breakdown under tangential airflow condition. For the C/SiC composite, the ablative evolution process of the microscopic structure and the formation and migration of silicon dioxide droplets in the edge region of the laser irradiation are clearly visible in the experimental images. The results show that the *in-situ* observation technology can also be used to observe the ablative behavior of composite materials. Different braided structures can influence the ablative behavior and ablation depth. The ablation depth of the 2D C/SiC composite was 1.13 mm, whereas that of the 3DN C/SiC composite was 1.23 mm. Compared with the 2D C/SiC composite, the 3DN C/SiC composite exhibits higher thermal conductivity in the thickness direction, resulting in a significantly higher temperature than that of the 2D C/SiC composite; therefore, its thermochemical ablation rate is also higher than that of 2D C/SiC. The instantaneous ablation depths of the CFRP were obtained using PIVlab. The results showed apparent nonlinear behavior. The laser ablation depth of a CFRP composite under supersonic tangential airflow is related to the laser power density and airflow velocity. The ablation depth is 0.36 mm when the laser power density is 1273 W/cm², and the airflow velocity is Mach number of 1.8. When the airflow velocity increases to Mach number of 3.0, the ablation depth increases to 0.47 mm. When the laser power density increased to 2546 W/cm², the ablation depth increased to 1.07 mm. These results indicate that the laser power density has a strong influence on the laser ablation depth.

Conclusions In this study, an *in-situ* observation technology of laser-irradiated high-temperature is proposed, and the instantaneous ablative morphology of metals and composite materials exposed to laser and supersonic tangential airflow is obtained. Real-time ablative data were calculated using image processing methods. The flow of molten metals in the wake zone and the diffusive characteristics of the heat-affected zone were obtained using the Horn-Schunck optical flow method. The ablative behaviors of the composites were related to the braided structure of the reinforced phase. The mechanical ablation effect of the 2D C/SiC composite is mainly sheet-like ablation, whereas the behaviors of the 3DN C/SiC and CFRP composites are mainly fiber-by-layer ablation. The instantaneous ablation depths of the CFRP composites were obtained using PIV method. The results show that the *in-situ* observation technology proposed in this study has broad application prospects in extreme high-temperature engineering, especially in the study of laser damage effects.

Key words laser technique; laser damage effect; *in-situ* observation technology; instantaneous ablative morphology; supersonic tangential airflow; optical flow method